NANO LETTERS

pubs.acs.org/NanoLett

Letter

Doping Independent Work Function and Stable Band Gap of Spinel Ferrites with Tunable Plasmonic and Magnetic Properties

Nikhil Bhalla,* Shilpa Taneja, Preeti Thakur, Preetam Kumar Sharma, Davide Mariotti, Chiranjeevi Maddi, Oxana Ivanova, Dmitry Petrov, Alexander Sukhachev, Irina S. Edelman,* and Atul Thakur*

Cite This: *Nano Lett.* 2021, 21, 9780–9788

Read Online

ACCESS | Metrics & More | Article Recommendations | Supporting Information

ABSTRACT: Tuning optical or magnetic properties of nanoparticles, by addition of impurities, for specific applications is usually achieved at the cost of band gap and work function reduction. Additionally, conventional strategies to develop nanoparticles with a large band gap also encounter problems of phase separation and poor crystallinity at high alloying degree. Addressing the aforementioned trade-offs, here we report Ni–Zn nanoferrites with energy band gap (E_g) of ≈3.20 eV and a work function of ≈5.88 eV. While changes in the magnetoplasmonic properties of the Ni–Zn ferrite were successfully achieved with the incorporation of bismuth ions at different concentrations, there was no alteration of the band gap and work function in the developed Ni–Zn ferrite. This suggests that with the addition of minute impurities to ferrites, independent of their changes in the band gap and work function, one can tune their magnetic and optical properties, which is desired in a wide range of applications such as nanobiosensing, nanoparticle based catalysis, and renewable energy generation using nanotechnology.

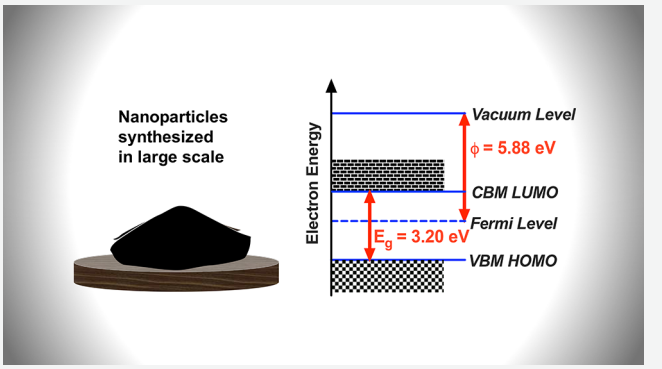

KEYWORDS: *plasmonics, magnetic, spinel, ferrites, atomic-doping, MCD*

Wide band gap semiconductor nanoparticles, with energy band gaps (E_g), enhance the performance of nanoscale devices in a wide range of applications ranging from deep-UV optoelectronics,[1] quantum computing,[2] biosensing,[3] high-power electronics,[4] to the use of nanoparticles in extreme environment applications. Engineering atoms to form nanoscale alloys is one of the main routes for achieving E_g modulation in nanoparticles.[5,6] For instance, several nanoalloys such as ZnO,[7] $ZnGa_2O_4$,[8] Ga_2O_3/SnO_2,[9] CuO,[10] GaOOH,[11] and many others[12] have been synthesized recently with unique electrical and optical properties. Among these materials the spinel compounds (such as $ZnGa_2O_4$) possess structural features which are suitable for tuning the optoelectronic properties of the material at nanoscale.[13] This is due to the inherent nature of the spinel configuration which allows a deserved choice of cation coordination within the structure of these materials.[14,15] This flexibility in the choice of cation also allows tuning of the dielectric and magnetic (in the case of spinel ferrites) properties of the spinel materials.[16−19] More specifically, the spinel ferrites have a general structural formula AB_2O_4 where A and B are divalent and trivalent cations, respectively.[20] Depending on the choice of cations and external conditions such as temperature or pressure, the distribution of the cations within the tetrahedral and octahedral positions in the structure can be changed.[21,22] This distribution of the cations is further defined by the degree of inversion (x) which is represented as $(A_{1-x}B_x)[A_xB_{2-x}]O_4$ where the value of x varies from 0 to 1. Note that the material structure for $x = 0$ is called a normal spinel, for $x = 1$, it is an inverse spinel, while for $x = 2/3$, the structure is known as a random spinel structure.[23] We can consider this process of changing the degree of inversion as the nanoparticle doping process. To change the degree of inversion, various physical and chemical techniques such as sol–gel, combustion, hydrothermal, and coprecipitation methods can be utilized to achieve doped nanoparticles with uncommon optoelectronic properties.[24] For example, increase in conductivity, enhancement in the magnetic moment, and nuclear magnetic properties, including hyperfine field distributions, isomer shifts, and quadrupole interactions,[25] can be achieved by doping the nanoparticle. Most often such

Received: September 29, 2021
Revised: October 27, 2021
Published: November 4, 2021

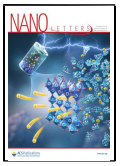

https://doi.org/10.1021/acs.nanolett.1c03767
Nano Lett. 2021, 21, 9780–9788

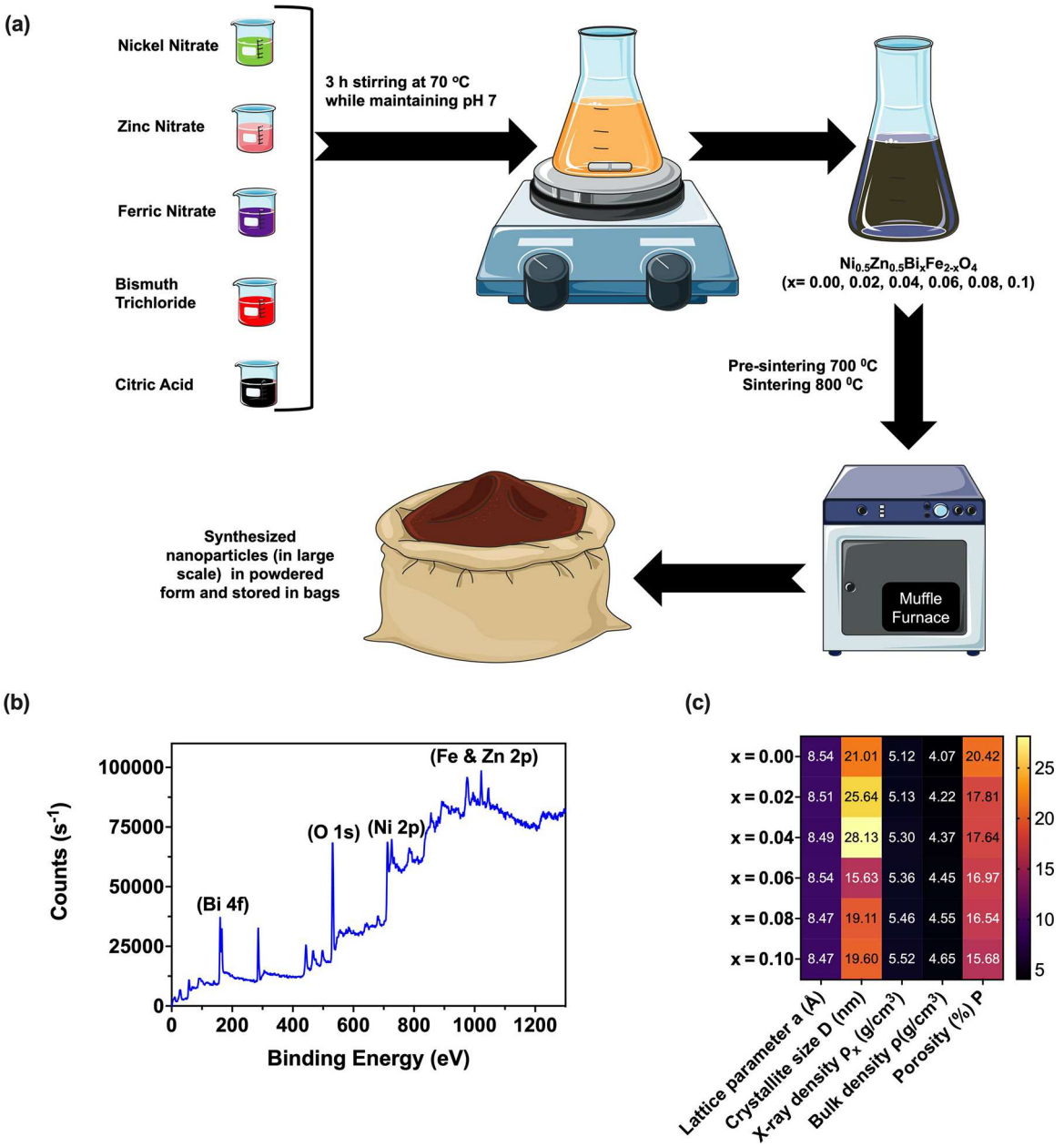

Figure 1. Schematic and nanoparticle characterization: (a) Steps of fabrication where salt solutions are mixed together and heated while maintaing a constant pH and temperature. Thereafter, post combustion the particle mixture is sinterted at high temperature to yield spinel nanoparticles. (b) XPS spectrum of the developed nanoparticles (x = 0.06 is shown here, XPS for other dopant concentrations are provided in the Supporting Information). (c) Detailed survey of the elemental properties identified within the XRD, confirming the chemical identity of the spinel nanoparticles. Note that in later figures 0.00−0.10 dopant concentrations are referred to as S1−S6 samples. Note that some components of the schematic in part a are incorporated from free to use art available on smart.servier.com.

changes are necessary for fine-tuning the application of the developed nanoparticle for a specific purpose. For instance within application of semiconductor nanoparticles (such as our spinel nanoparticles) associated with the photocatalysis, it is of utmost importance that the free electron hole pairs are generated.[26,27] Therefore, the necessary condition for it to be a photocatalyst is the low recombination rate which can be easily tuned by adding dopant or changing its concentration through modulation in the degree of inversion. Similarly, for nano-plasmonic biosensing, such as surface enhanced Raman spectroscopy (SERS) or localized surface plasmon resonance (LSPR), application of the degree in inversion can lead to enhanced sensitivity, surface stability, and reproducibility in multimetallic or semiconductor like LSPR platforms.[28−30]

In this context, we have developed bismuth (Bi) doped nickel zinc (Ni−Zn) spinel ferrite nanopartciles, $Ni_{0.5}Zn_{0.5}Bi_xFe_{2-x}O_4$, where x is the degree of inversion, varying from 0.00 to 0.1 in steps of 0.02. We characterized the developed material with physical, optical, magnetic, and atomic resolution tools to understand the features of the developed material. We find that the optical band gap and work function of the material do not change with the degree of inversion while the magnetic and plasmonic properties' (optical properties in UV−vis) regions change with changes in the degree of inversion. This suggests that the optomagnetic

https://doi.org/10.1021/acs.nanolett.1c03767
Nano Lett. 2021, 21, 9780−9788

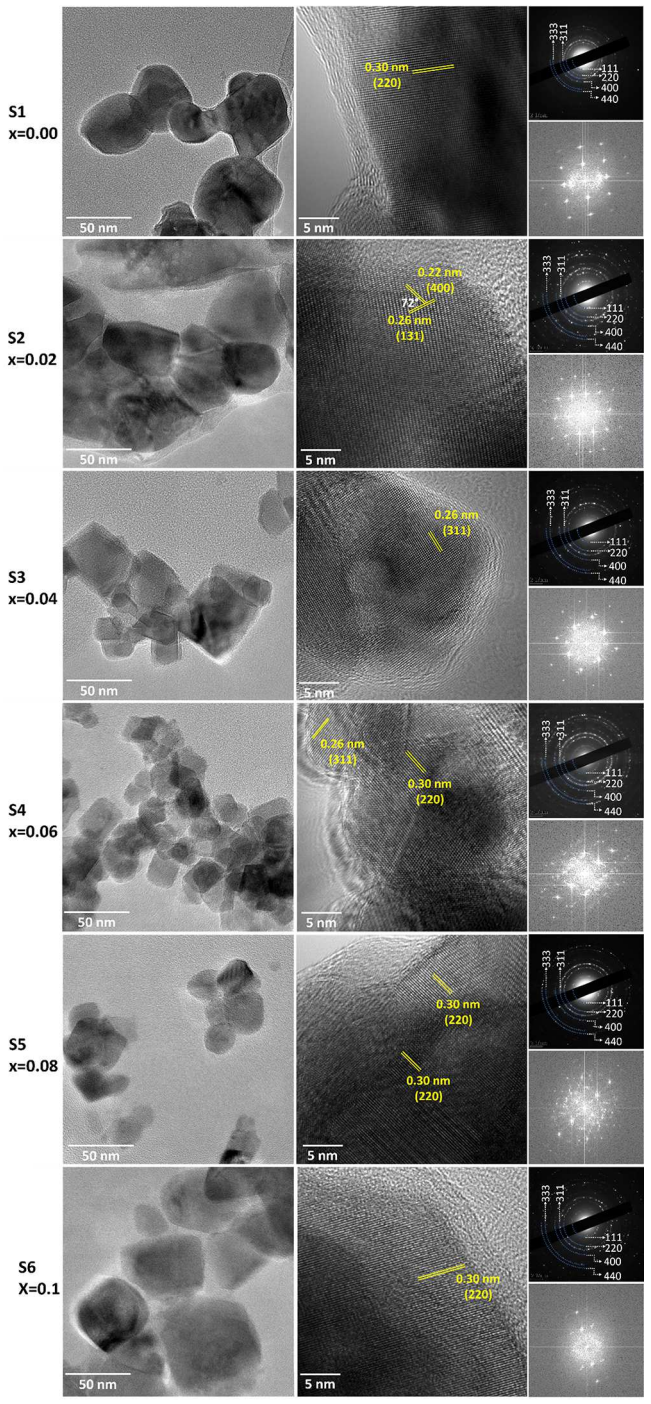

Figure 2. HRTEM of spinel nanoparticles: Within this figure panels S1−S6 correspond to the 6 sets of nanoparticles developed with different Bi dopant concentrations. Apart from the high-resolution imaging, the figure also shows the selected area electron diffraction patterns and FFT for the samples.

properties of the developed material are tunable without including the effects of dopant which also generally changes the optical band gap of the material. Achieving the optical gap (E_g) is one of the fundamental issues in achieving controllable and purposeful optoelectronic properties in the wide wavelength range of semiconductors.[31] Therefore, the results discussed here serve as a guide in the development and discovery of materials with unique properties.

The $Ni_{0.5}Zn_{0.5}Bi_xFe_{2-x}O_4$ nanoparticles were synthesized by the citrate precursor method where aqueous solutions of zinc, nickel, bismuth, and iron salts were dissolved with citric acid to create a homogneous solution. This solution was then sintered at low temperatures to yield nanoparticles in the powered form. The schematic in Figure 1a shows the process of synthesis, and detailed steps are discussed in the methodology section. For simplicity, hereafter we will use x to refer to the relative concentrations of the precursor used in the synthesis. It should be noted that the process of nanoparticle preparation is simple, is cost-effective, and can generate particles in large scale within a short duration of time. The amount of particle generation is only limited by the size of the instrumentation involved—such as the size of the furnace, hot plate, magnetic stirrer, and beakers. After development of the nanoparticles, we carried out X-ray photoelectron spectroscopy (XPS); Figure 1b shows the low-resolution full scan XPS for $x = 0.06$, while XPS for all other dopant concentrations is shared in the Supporting Information. Essentially, the peaks correspond to the binding energies (BEs) of Bi 4f, Ni 2p, Zn 2p, Fe 2p, and O 1s.[32−35] The BEs of Bi 4f, Ni 2p, Zn 2p, and Fe 2p are ascribed to the BEs of the Bi^{3+}, Ni^{2+}, Zn^{2+}, and Fe^{3+} ionic states in the samples. As observed in Figure 1b, the bismuth ion is found to have an oxidation state of +3 as the core level spectra for Bi 4f are in the ranges 158−160 eV and 164−166 eV for the 7/2 and 5/2 spin orbit doublet components, respectively. In the observation of the element iron, the Fe 2p states of the Fe atom could be used to distinguish the variation between Fe^{2+} and Fe^{3+}. The pure Fe 2p narrow scan (see the Supporting Information) shows two wide doublet peaks with spin−orbit splitting energies of 3.88 and 4.43 eV and positioned in the ranges 710−713 eV and 722−727 eV for Fe $2p_{3/2}$ and Fe $2p_{1/2}$, respectively. The peak with the range 710−713 eV is attributed to the Fe^{3+} cation located at the octahedral site in the spinel structure. The peak with the range 722−727 eV is due to the presence of Fe^{2+} cation located at the tetrahedral site in the spinel structure. In addition, we observe the nickel element in the ranges 854−856 eV and 863−874 eV, which correspond to the Ni $2p_{3/2}$ and Ni $2p_{1/2}$ electrons in the Ni^{2+} oxidation state, respectively. The presence of the element zinc is also confirmed by observation of the peak energies in the ranges 1020−1023 eV and 1044−1049 eV, which correspond to Zn $2p_{3/2}$ and Zn $2p_{1/2}$ electrons in the Zn^{2+} oxidation state, respectively. Note that the element bismuth also exists in the pentavalent state (Bi^{5+}) which can replace the few Fe^{2+} ions in the spinel nanoferrite structure that can further influence the magnetic and electrical properties of the nanoparticles. Furthermore, the spinel crystalline structure (AB_2O_4) with tetrahedral and octahedral sites for metal atoms is also confirmed by correlating the identified elements in the XPS with X-ray diffraction (XRD). Using XRD we also extract the lattice parameter, X-ray density, bulk material density, porosity, and crystalline size of the nanoparticles; see Figure 1c. We observe a decrease in the lattice parameter with addition of the dopant. In addition, the lattice parameter, bulk density, and X-ray density increase with the addition of Bi (at $x = 0.02$) and then decrease with further increase in the Bi concentration from $x = 0.02$ to 0.10. See the Supporting Information for the detailed XPS high-resolution scan and XRD of all nanoparticles. The changes in the aforementioned atomic properties identified using XRD are attributed to the changes in the phase of the material.[36]

https://doi.org/10.1021/acs.nanolett.1c03767
Nano Lett. 2021, 21, 9780−9788

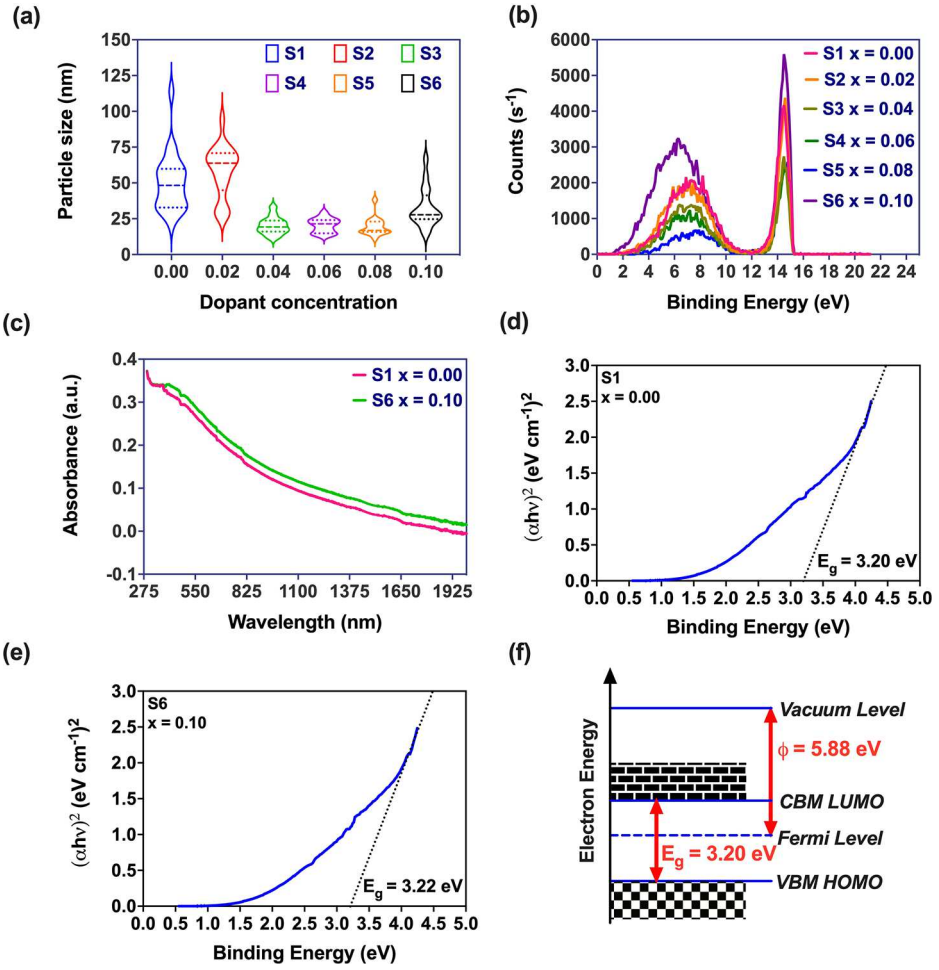

Figure 3. Nanoparticle physical and optical characteristics: (a) Violin plot with the particle size distribution in S1−S6. (b) Ultraviolet photoelectron spectroscopy of the magnetic nanoparticles S1−S6 (c) UV−vis absorbance spectroscopy of S1 and S6. (d and e) Tauc plot with the energy band gap for samples S1 and S6, respectively. (f) Optical band diagram of the nanoparticles.

Figure 2 shows the transmission electron microscopy (TEM) images for all six nanoparticles (S1 to S6). As shown in the images, the particles have dimensions in the nanorange. The particle size distribution extracted from the TEM characterization will be discussed later in Figure 3a. Figure 2 also shows the selected area electron diffraction patterns (SAED) for the samples. The *d*-spacing calculated from the SAED patterns matched well with the XRD patterns (see the Supporting Information for the XRD related data analysis). The SAED patterns with plane labels (marked in yellow) have been added in the figures. From SAED analysis, the spacings for all six samples are very similar and show no measurable differences. Within these high-resolution images, the lattice planes can also be observed. The calculated interplanar spacing was utilized for determination of the plane type, and based on the analysis of multiple HRTEM images from each of the samples (here only one HRTEM image is reported from each sample), a variety of planes are observed. For reporting purposes, HRTEM images with various identified planes are shown here. For instance, the interplanar spacing of 0.30 nm is measured, which corresponds to the 220 plane of the spinel cubic crystal in sample S1. For sample S2, lattice spacings of 0.26 nm (corresponding to the 311 plane) and 0.22 nm (corresponding to the 400 plane) of the spinel cubic crystal are observed. The interplanar angle of 72 degrees further confirms the identified planes. Similarly, for samples S3−6 the lattice spacings corresponding to cubic spinel planes are identified as 311 and 220 (marked in yellow within the images). Additionally, the fast Fourier transform (FFT) corresponding to the planar area indicates sharp patterns asserting the highly crystalline nature of the prepared nanoparticles.

The work function of the nanoparticles was calculated using ultraviolet photoelectron spectroscopy (UPS). UPS allows us to investigate materials within 3.10−124 eV energy, which is ideal for the investigation of valence and conduction band electrons. Empirically the work function (φ) can be calculated from the UPS measurements according to the relation $\varphi = h\nu - E_{cutoff}$, where $h\nu$ is the excitation energy source (He I 21.22 eV) and E_{cutoff} is the energy cutoff measured from the UPS spectra (Figure 3b). UPS measurements produced the value ≈5.88 eV for all our samples. From Figure 3b, the energy cutoff is measured as 15.34 eV (W) for all six samples. Therefore, the difference between excitation energy sources was measured to be 5.88 eV. It should be noted that despite the change in concentration of the dopant from 0.00 to 0.10 and differences in morphology (different sizes of the nanoparticles as seen in Figure 3a) this value does not change, validating our observation that the developed nanoparticles have a work function which is independent of the dopant concentration. This is in contrast with the reports in the

https://doi.org/10.1021/acs.nanolett.1c03767
Nano Lett. 2021, 21, 9780−9788

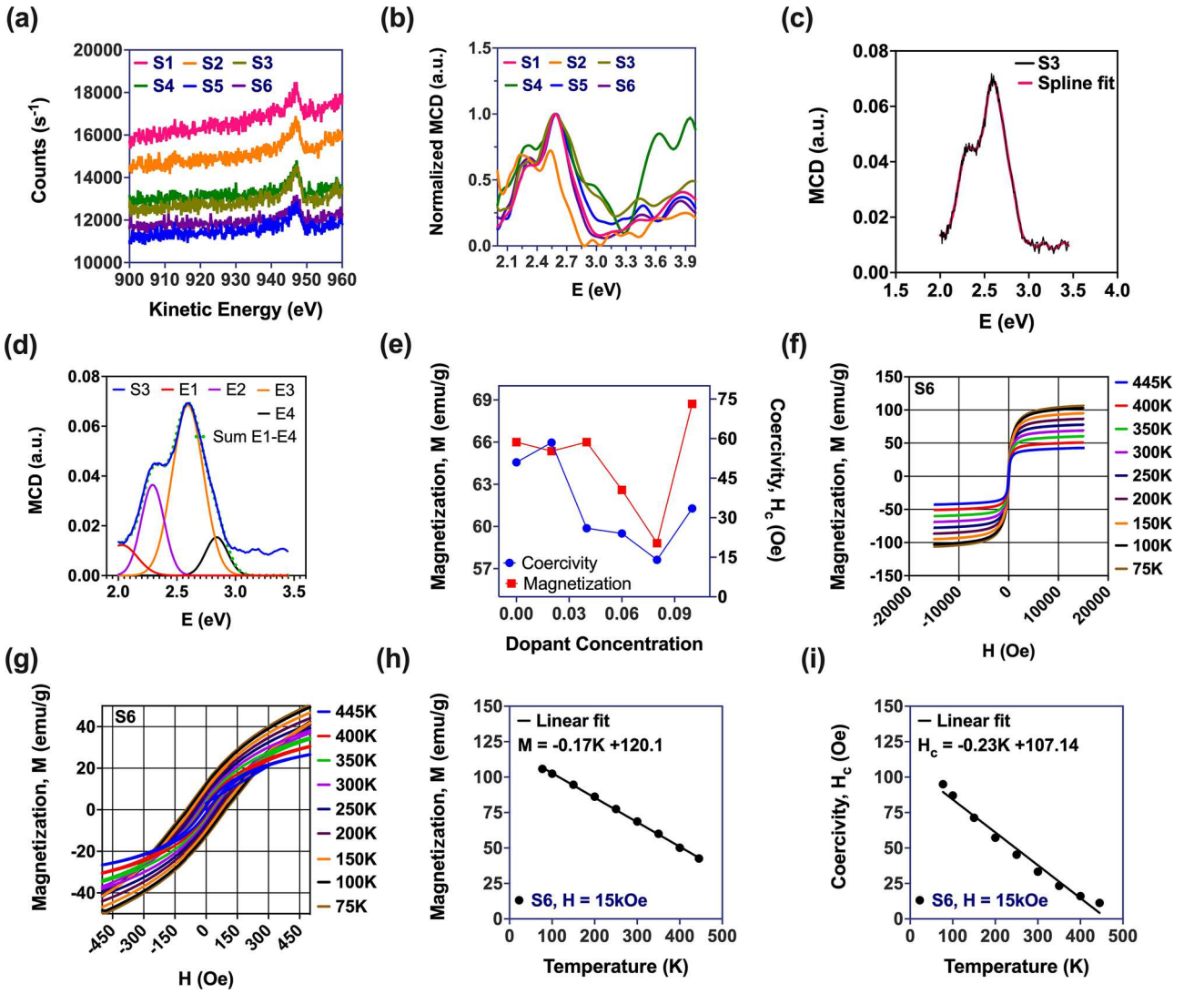

Figure 4. Nanoparticle optical and magnetic characterization: (a) Reflection electron energy loss spectroscopy (REELS). (b) Normalized MCD spectra for S1−S6 samples at 300 K. (c) MCD spectrum of sample 3 at 300 K. (d) Spectrum deconvolution to the Gaussian components. (e) Variation of coercivity and magnetization with change in dopant concentration. (f and g) Changes in magnetization with change in temperature from 75 K to 445 K. The variation in coercivity and magnetization with temperature is ploted in parts h and i, respectively.

literature where adding metallic dopant either increases[37] or decreases[38] the work function of a given nanomaterial. To further validate the independence of the band structure of the material on the dopant concentration, we calculate the band gap of the developed nanoparticles. To determine the band gap of the samples, we performed UV−vis spectroscopy of all samples. The absorbance spectra of all six samples are found to be identical, and minute differences in the absorption, which are not easy to distinguish, are observed. Therefore, we only show samples S1 and S6, between which the absorbances of the S2−S5 samples exist, in Figure 3c−e. To calculate the band gaps of the samples, the experimental absorbance spectra were reduced to the form $(a*E)^2 = f(E)$, where the frequency dependence of the absorption coefficient in the vicinity of the absorption edge is described by $a = [C(E - E_g)^{1/2}]/E$. In this equation, a is the absorption coefficient (here we use aborbance A, proportional to the absorption coefficient), E is the photon energy, E_g is the optical band gap, and C is a constant.[39]

The band gap values were determined by extrapolating the straight sections of the obtained curves in the short-wavelength region of the spectrum. From the analysis, we observe that the band gap of the sample containing no Bi dopant is 3.20 eV, and by increasing the Bi concentration, the band gap increases to a maximum of ≈3.22 eV (in sample S6). As the observed change in the band gap is less than 0.5%, we can consider it to be relatively independent of the concentration of the Bi dopant. A general band diagram of the nanoparticles is shown in Figure 3f where the band gap is shown as 3.20 eV and the work function is 5.88 eV.

Figure 4 a shows the magnetic and optical characterization of the developed spinel nanoparticles. Prior to the discussion in Figure 4, we would like to mention that using the unpolarized light, we observe a wide absorbance region in the UV−vis spectrum; see Figure 3c−e. In addition, the kinetic energy measured in UPS, Figure 3b, can also be attributed to the molecular electronic absorptions within 2−20 eV—primarily due to the plasmon excitation, both bulk and surface plasmon. The bulk plasmon consists of longitudinal waves and in the

https://doi.org/10.1021/acs.nanolett.1c03767
Nano Lett. 2021, 21, 9780−9788

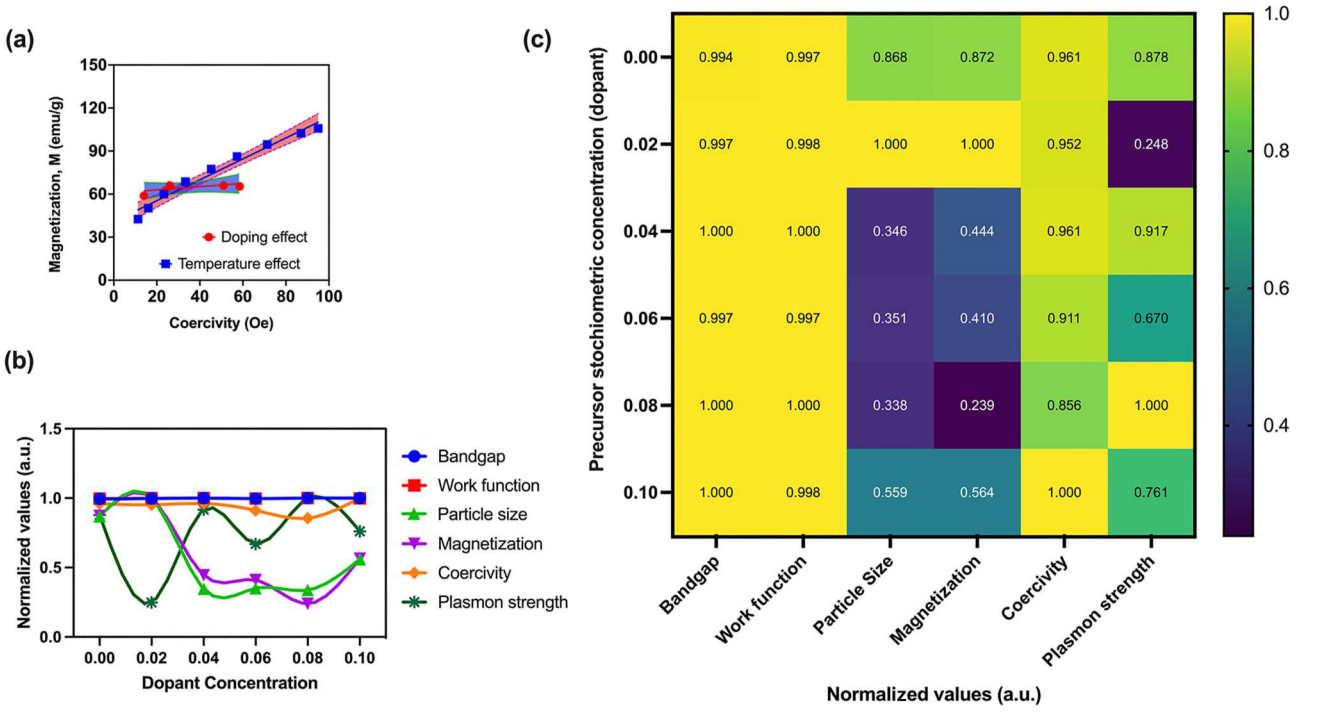

Figure 5. Corelation between the properties of the nanoparticle: (a) Plot showing how doping and temperature change the relationship between the magnetization and coercivity of the developed ferrite. A linear relationship is demonstrated by linear regression analysis where both blue and red lines show the regression coefficient $R^2 > 0.97$. The data also shows the 95% confidence bands of the fitted line. (b) Normalized variant vs dopant concentration plot indicating that the band gap and work function do not change with the degree of inversion. (c) Heat map showing the corelation between the properties. In a given column less variation in the color indicates less variation in particles with variation in dopant concentration.

surface plasmons, where we have half the energy of the bulk plasmons, constitutes the transverse wave. To confirm that these plasmonic effects were contributed by the Bi dopant, we study the inner shell ionization in the reflection mode using reflection electron energy loss spectroscopy (REELS). REELS provides information on the electron transport phenomena in the surface of a solid, where incident electrons are elastically scattered through an interaction with the material's valence and core electrons, providing direct insight into the elemental information. The REELS spectra, in Figure 4a, were measured at TOAs (take off angles) of 90° for different inversion values of the spinel nanoparticle. The spectra are magnified 2 times relative to the no-loss peaks. The analyzer transfer function, which is proportional to the kinetic energy of the electrons, has also been removed, and therefore the lines represent the experimental spectra. Analyzing these peaks, the REELS has generated complementary results to XPS in Figure 1b, where the peak at 946.63 eV can be correlated with the precursor concentration, the x = 0.00−0.10 value of bismuth. These peaks are commonly observed as satellite peaks for atoms in ferrite based alloys.[40]

To study the effect of polarized light, we investigate differential absorption of left and right circular polarized light using magnetic circular dichroism (MCD); see Figure 4b. Here we observe that the shapes of the MCD spectra for all the samples are similar (less than 10% variation in the peak locations), except for sample 2 (x = 0.02), which has a large deviation in its MCD properties. This is an anomaly which we attribute to the fact that the size of the particles in the x = 0.2 sample was much larger than the other doped nanoparticles, as seen from the TEM characterization. Moreover, a quantitative comparison of the signal intensity for all samples is presumptive because it is nontrivial to accurately determine the total thickness of the nanoparticles along the path of the light beam through the sample. However, the constancy in the shape of the MCD spectrum indicates that the substitution of Bi for Fe ions in the concentrations used does not affect the electronic structure of Ni−Zn-ferrite nanocrystals. Therefore, here we only analyze sample 3 (S3) in detail to represent and discuss the features of the developed nanoparticles. The obtained MCD for S3 is shown in Figure 4c and d. The MCD spectrum shape is similar to that of the maghemite (γ-Fe_2O_3) thin film in our previous work.[41] This is not surprising since both compounds contain Fe^{3+} ions of the $3d^5$ ion configuration in the octahedral and tetrahedral positions. The experimental spectrum is also decomposed into individual components of Gaussian shape in Figure 4d. The best fit of the calculated spectrum to the experimental one is obtained taking into account four components with energies E1−E4 = 2.023, 2.288, 2.590, and 2.839 eV, respectively. By analogy with maghemite, the strongest peaks E2 and E3 can be related to the electronic transitions from the ground states of the Fe^{3+} ion $^6A_{1g}(^6S_g)$ in the octahedral and $^6A_1(^6S)$ in the tetrahedral sites to the excited states: $^4A_{1g}$,$^4E_g(^4G)$ and $^4A_1$,$^4E(^4G)$. Since the characterization is performed in the UV−vis range, the absorbance properties of the material toward polarized light are attributed to the surface and bulk plasmons as indicated earlier in our discussion.

Magnetic properties are reported here in Figure 4e−i. The saturation magnetization (M_s) and coercivity (H_c) depend on both Bi concentration and nanoparticle average size; see Figure 4e for the dopant concentration, which affects the particle as seen from Figure 3a. Indeed, in samples 3−5, the nanoparticle size is approximately the same or less as compared to samples

https://doi.org/10.1021/acs.nanolett.1c03767
Nano Lett. 2021, 21, 9780−9788

1, 2, and 6. In the developed nanoparticle series (3−5), a decrease in the H_c is observed with a linear trend that changes with increase in the Bi concentration. The minimal H_c value (14 Oe) observed in our sample 5 is rather attractive for a wide range of high-frequency applications. Detailed curves for extraction of these M_s and H_c are shared in the Supporting Information for all 6 samples. We also investigate the effect of temperature on M_s and H_c; see Figure 4f−i, which indicates a linear drop in the values when temperature is varied from 77 K to 445 K.

We found a linear relationship between magnetization and coercivity; see Figure 5 a. While the relationship between magnetization and coercivity might be linear, it should not be generalized for all nanomaterials as we have only found this linear relationship for our developed ferrite. Figure 5 b correlates the nanoparticle properties with the dopant concentration. Note that within Figure 5b, the data sets used for ploting the curves are normalized with respect to the largest data value in that particular data set. This leads to a dimensionless number which is represented as a normalized value with arbitrary units in the *y*-axis, further elucidating the comparison between the various properties of the materials with a change in the degree of the inversion. Clearly, Figure 5b shows that the optical band gap and work function do not vary with the change in the dopant concentration (less than 1% changes observed). Variations up to 17% are observed in the coercivity, and more than 70% variations are in the magnetization, plasmonic strength, and particle size when the dopant concentration is changed. Note that these variations are the maximum changes of the values with a given data set, i.e. the difference between the highest and lowest values, which are calculated as a percentage change with respect to the lowest value in the data set. We further find the correlation between the normalized values that change within the given data set, and these are represented in the form of a heat map in Figure 5c. This heat map again suggests that there are insignificant changes within the band gap and work function with a change in the dopant concentration. The fabrication process is optimized for uniform, homogeneous, and stoichiometric nanoferrites. The different parameters such as quantity of distilled water used, citric acid as fuel, presintering, sintering temperature, and heating and cooling rates were all optimized for the reproducible results discussed here.

In summary, we have proposed a state-of-the-art design concept for the spinel nanoferrites which have tunable magnetic and plasmonic properties but stable optical band gap and work function. These ferrites were made up of Ni and Zn elements, and to achieve the tunable optomagnetic properties, Bi was inserted within the compound. To reveal the aforementioned unique properties, we performed several physiochemical, magnetic, and optical characterizations including REELS and MCD performed for the first time in Ni−Zn spinel ferrites. This work would open up a new avenue to develop wide band gap nanomaterials possessing specifically tailored optomagnetic properties, which have been facing the challenge of band gap reduction with increase in property enhancing dopants.

■ ASSOCIATED CONTENT

Supporting Information

The Supporting Information is available free of charge at https://pubs.acs.org/doi/10.1021/acs.nanolett.1c03767.

Detailed information on XPS, XRD, vibrating sample magnetometer (VSM) measurements, MCD, and methods used for nanoparticle preparation and characterization (PDF)

■ AUTHOR INFORMATION

Corresponding Authors

Nikhil Bhalla − *Nanotechnology and Integrated Bioengineering Centre (NIBEC), School of Engineering, Ulster University, Jordanstown BT37 0QB Northern Ireland, United Kingdom; Healthcare Technology Hub, Ulster University, Jordanstown BT37 0QB Northern Ireland, United Kingdom;* orcid.org/0000-0002-4720-3679; Email: n.bhalla@ulster.ac.uk

Irina S. Edelman − *L.V. Kirensky Institute of Physics, Siberian Branch of RAS, 660036 Krasnoyarsk, Russia;* orcid.org/0000-0002-5589-6559; Email: ise@iph.krasn.ru

Atul Thakur − *Amity Institute of Nanotechnology, Amity University Haryana, Gurugram, Haryana 122413, India*; Email: athakur1@ggn.amity.edu

Authors

Shilpa Taneja − *Department of Physics, Amity University Haryana, Gurugram, Haryana 122413, India*

Preeti Thakur − *Department of Physics, Amity University Haryana, Gurugram, Haryana 122413, India*

Preetam Kumar Sharma − *Nanotechnology and Integrated Bioengineering Centre (NIBEC), School of Engineering, Ulster University, Jordanstown BT37 0QB Northern Ireland, United Kingdom; Healthcare Technology Hub, Ulster University, Jordanstown BT37 0QB Northern Ireland, United Kingdom; Department of Chemical Engineering, Loughborough University, Loughborough LE11 3TU, United Kingdom;* orcid.org/0000-0002-5694-8445

Davide Mariotti − *Nanotechnology and Integrated Bioengineering Centre (NIBEC), School of Engineering, Ulster University, Jordanstown BT37 0QB Northern Ireland, United Kingdom;* orcid.org/0000-0003-1504-4383

Chiranjeevi Maddi − *Nanotechnology and Integrated Bioengineering Centre (NIBEC), School of Engineering, Ulster University, Jordanstown BT37 0QB Northern Ireland, United Kingdom*

Oxana Ivanova − *L.V. Kirensky Institute of Physics, Siberian Branch of RAS, 660036 Krasnoyarsk, Russia*

Dmitry Petrov − *L.V. Kirensky Institute of Physics, Siberian Branch of RAS, 660036 Krasnoyarsk, Russia*

Alexander Sukhachev − *L.V. Kirensky Institute of Physics, Siberian Branch of RAS, 660036 Krasnoyarsk, Russia*

Complete contact information is available at: https://pubs.acs.org/10.1021/acs.nanolett.1c03767

Notes

The authors declare no competing financial interest.

■ ACKNOWLEDGMENTS

All authors would like to acknowledge support from EPSRC fund, award no. EP/R008841/1. Nikhil Bhalla wishes to thank Department of Economy, Northern Ireland, for supporting part of this work under GCRF Pump Priming Fund. Additionally, Atul Thakur and Preeti Thakur would like to acknowledge Gurujal, an initiative with district administration Gurugram for financial assistance from project no.176, Amity

Incubation grant from the Ministry of Electronics and Information Technology (MeitY) under Technology Incubation and Development of Entrepreneurs (TIDE 2.0) program and the startup nanoLatticeX.

REFERENCES

(1) Sutter, E.; French, J. S.; Sutter, S.; Idrobo, J. C.; Sutter, P. Vapor-liquid-solid growth and optoelectronics of gallium sulfide van der Waals nanowires. *ACS Nano* **2020**, *14*, 6117−6126.
(2) Kabashin, A. V.; Singh, A.; Swihart, M. T.; Zavestovskaya, I. N.; Prasad, P. N. Laser-processed nanosilicon: a multifunctional nanomaterial for energy and healthcare. *ACS Nano* **2019**, *13*, 9841−9867.
(3) Lah, N. A.; Zubir, M. N.; Mahendran, A.; Samykano, L. In *Engineered nanomaterial in electronics and electrical industries*; Hussain, C. M., Ed.; Elsevier, 2018; pp 324−364.
(4) Pearton, S. J.; Norton, D. P.; Ren, F. The Promise and Perils of Wide-Bandgap Semiconductor Nanowires for Sensing, Electronic, and Photonic Applications. *Small* **2007**, *3*, 1144−1150.
(5) Zhang, S.; Xu, R.; Luo, N.; Zou, X. Two-dimensional magnetic materials: structures, properties and external controls. *Nanoscale* **2021**, *13*, 1398−1424.
(6) Wu, Z.-P.; et al. Alloying-realloying enabled high durability for Pt-Pd-3d-transition metal nanoparticle fuel cell catalysts. *Nat. Commun.* **2021**, *12*, 1−14.
(7) Xie, A.; Yang, D.; Li, X.; Zeng, H. Lattice restraint induced ultra-large bandgap widening of ZnO nanoparticles. *J. Mater. Chem. C* **2019**, *7*, 8969−8974.
(8) Chikoidze, E.; et al. p-type ultrawide-band-gap spinel ZnGa2O4: New perspectives for energy electronics. *Cryst. Growth Des.* **2020**, *20*, 2535−2546.
(9) Dong, H.; et al. Ultrawide Band Gap Oxide Semiconductor-Triggered Performance Improvement of Perovskite Solar Cells via the Novel Ga2O3/SnO2 Composite Electron-Transporting Bilayer. *ACS Appl. Mater. Interfaces* **2020**, *12*, 54703−54710.
(10) Dixit, T.; Tripathi, A.; Solanke, S. V.; Ganapathi, K. L.; Rao, M. R.; Singh, V. Ultra-Wide Bandgap Copper Oxide: High Performance Solar-Blind Photo-detection. *IEEE Electron Device Lett.* **2020**, *41*, 1790−1793.
(11) Upadhyay, D.; Joshi, N.; Jha, P. K. Two dimensional hexagonal GaOOH: A promising ultrawide bandgap semiconductor for smart optoelectronic applications. *Chem. Phys. Lett.* **2021**, *765*, 138310.
(12) Xie, C.; Lu, X.-T.; Tong, X.-W.; Zhang, Z.-X.; Liang, F.-X.; Liang, L.; Luo, L.-B.; Wu, Y.-C. Recent progress in solar-blind deep-ultraviolet photodetectors based on inorganic ultrawide bandgap semiconductors. *Adv. Funct. Mater.* **2019**, *29*, 1806006.
(13) Shen, Y.-C.; Tung, C.-Y.; Huang, C.-Y.; Lin, Y.-C.; Lin, Y.-G.; Horng, R.-H. Study on Optoelectronic Characteristics of ZnGa2O4 Thin-Film Phototransistors. *ACS Applied Electronic Materials* **2019**, *1*, 783−788.
(14) Zhou, Y.; Sun, S.; Xi, S.; Duan, Y.; Sritharan, T.; Du, Y.; Xu, Z. J. Superexchange Effects on Oxygen Reduction Activity of Edge-Sharing [CoxMn1- xO6] Octahedra in Spinel Oxide. *Adv. Mater.* **2018**, *30*, 1705407.
(15) Duan, Y.; Sun, S.; Sun, Y.; Xi, S.; Chi, X.; Zhang, Q.; Ren, X.; Wang, J.; Ong, S. J. H.; Du, Y.; Gu, L.; Grimaud, A.; Xu, Z. J. Mastering surface reconstruction of metastable spinel oxides for better water oxidation. *Adv. Mater.* **2019**, *31*, 1807898.
(16) Venturini, J.; Tonelli, A. M.; Wermuth, T. B.; Zampiva, R. Y. S.; Arcaro, S.; Viegas, A. D. C.; Bergmann, C. P. Excess of cations in the sol-gel synthesis of cobalt ferrite (CoFe2O4): A pathway to switching the inversion degree of spinels. *J. Magn. Magn. Mater.* **2019**, *482*, 1−8.
(17) Andersen, H. L.; Granados-Miralles, C.; Saura-Múzquiz, M.; Stingaciu, M.; Larsen, J.; SØndergaard-Pedersen, F.; Ahlburg, J. V.; Keller, L.; Frandsen, C.; Christensen, M. Enhanced intrinsic saturation magnetization of Zn x Co 1- x Fe 2 O 4 nanocrystallites with metastable spinel inversion. *Materials Chemistry Frontiers* **2019**, *3*, 668−679.
(18) Wu, L.; Lu, Y.; Shao, W.; Wei, H.; Tong, G.; Wu, W. Simple Salt-Template Assembly for Layered Heterostructures of C/Ferrite and EG/C/MFe2O4 (M= Fe, Co, Ni, Zn) Nanoparticle Arrays toward Superior Microwave Absorption Capabilities. *Adv. Mater. Interfaces* **2020**, *7*, 2000736.
(19) Xiong, P.; Bai, P.; Li, A.; Li, B.; Cheng, M.; Chen, Y.; Huang, S.; Jiang, Q.; Bu, X.-H.; Xu, Y. Bismuth Nanoparticle@ Carbon Composite Anodes for Ultralong Cycle Life and High-Rate Sodium-Ion Batteries. *Adv. Mater.* **2019**, *31*, 1904771.
(20) Mohapatra, J.; Zeng, F.; Elkins, K.; Xing, M.; Ghimire, M.; Yoon, S.; Mishra, S. R.; Liu, J. P. Size-dependent magnetic and inductive heating properties of Fe 3 O 4 nanoparticles: scaling laws across the superparamagnetic size. *Phys. Chem. Chem. Phys.* **2018**, *20*, 12879−12887.
(21) Narang, S. B.; Pubby, K. Nickel spinel ferrites: A review. *J. Magn. Magn. Mater.* **2021**, *519*, 167163.
(22) Catalan, G.; Scott, J. F. Physics and applications of bismuth ferrite. *Adv. Mater.* **2009**, *21*, 2463−2485.
(23) Andersen, H. L.; Saura-Múzquiz, M.; Granados-Miralles, C.; Canévet, E.; Lock, N.; Christensen, M. Crystalline and magnetic structure-property relationship in spinel ferrite nanoparticles. *Nanoscale* **2018**, *10*, 14902−14914.
(24) Thakur, P.; Chahar, D.; Taneja, S.; Bhalla, N.; Thakur, A. A review on MnZn ferrites: Synthesis, characterization and applications. *Ceram. Int.* **2020**, *46*, 15740−15763.
(25) Granone, L. I.; Ulpe, A. C.; Robben, L.; Klimke, S.; Jahns, M.; Renz, F.; Gesing, T. M.; Bredow, T.; Dillert, R.; Bahnemann, D. W. Effect of the degree of inversion on optical properties of spinel ZnFe 2 O 4. *Phys. Chem. Chem. Phys.* **2018**, *20*, 28267−28278.
(26) Kim, Y.; Smith, J. G.; Jain, P. K. Harvesting multiple electron-hole pairs generated through plasmonic excitation of Au nanoparticles. *Nat. Chem.* **2018**, *10*, 763−769.
(27) Dojcinovic, M. P.; Vasiljevic, Z. Z.; Pavlovic, V. P.; Barisic, D.; Pajic, D.; Tadic, N. B.; Nikolic, M. V. Mixed Mg-Co spinel ferrites: Structure, morphology, magnetic and photocatalytic properties. *J. Alloys Compd.* **2021**, *855*, 157429.
(28) Tan, C. F.; Zin, A. K. S. S.; Chen, Z.; Liow, C. H.; Phan, H. T.; Tan, H. R.; Xu, Q.-H.; Ho, G. W. Inverse stellation of CuAu-ZnO multimetallic-semiconductor nanostartube for plasmon-enhanced photocatalysis. *ACS Nano* **2018**, *12*, 4512−4520.
(29) Jin, R.; Pei, Y.; Tsukuda, T. Controlling nanoparticles with atomic precision. *Acc. Chem. Res.* **2019**, *52*, 1−1.
(30) Pietrzak, M.; Ivanova, P. Bimetallic and multimetallic nanoparticles as nanozymes. *Sens. Actuators, B* **2021**, *336*, 129736.
(31) Ruddy, D. A.; Johnson, J. C.; Smith, E. R.; Neale, N. R. Size and bandgap control in the solution-phase synthesis of near-infrared-emitting germanium nanocrystals. *ACS Nano* **2010**, *4*, 7459−7466.
(32) Nesbitt, H. W.; Legrand, D.; Bancroft, G. M. Interpretation of Ni2p XPS spectra of Ni conductors and Ni insulators. *Phys. Chem. Miner.* **2000**, *27*, 357−366.
(33) Bera, S.; Prince, A. A. M.; Velmurugan, S.; Raghavan, P. S.; Gopalan, R.; Panneerselvam, G.; Narasimhan, S. V. Formation of zinc ferrite by solid-state reaction and its characterization by XRD and XPS. *J. Mater. Sci.* **2001**, *36*, 5379−5384.
(34) Nascimento, V. B.; Carvalho, V. D.; Paniago, R.; Soares, E. A.; Ladeira, L. O.; Pfannes, H. D. XPS and EELS study of the bismuth selenide. *J. Electron Spectrosc. Relat. Phenom.* **1999**, *104*, 99−107.
(35) Ricca, A.; Bauschlicher, C. W. J. Successive binding energies of Fe (CO) 5+. *J. Phys. Chem.* **1994**, *98*, 12899−12903.
(36) Jiang, M.; Berciu, M.; Sawatzky, G. A. Critical nature of the Ni spin state in doped NdNiO 2. *Phys. Rev. Lett.* **2020**, *124*, 207004.
(37) Kwon, K. C.; Choi, K. S.; Kim, S. Y. Increased work function in few-layer graphene sheets via metal chloride doping. *Adv. Funct. Mater.* **2012**, *22*, 4724−4731.
(38) Kwon, K. C.; Choi, K. S.; Kim, B. J.; Lee, J.-L.; Kim, S. Y. Work-function decrease of graphene sheet using alkali metal carbonates. *J. Phys. Chem. C* **2012**, *116*, 26586−26591.

https://doi.org/10.1021/acs.nanolett.1c03767
Nano Lett. 2021, 21, 9780−9788

(39) Makula, P.; Pacia, M.; Macyk, W. How to correctly determine the band gap energy of modified semiconductor photocatalysts based on UV-Vis spectra. *J. Phys. Chem. Lett.* **2018**, *9*, 6814−6817.
(40) Zhu, J.; Zhu, Z.; Zhang, H.; Lu, H.; Qiu, Y. Efficient degradation of organic pollutants by peroxymonosulfate activated with MgCuFe-layered double hydroxide. *RSC Adv.* **2019**, *9*, 2284−2291.
(41) Ivanova, O. S.; Ivantsov, R. D.; Edelman, I. S.; Petrakovskaja, E. A.; Velikanov, D. A.; Zubavichus, Y. V.; Zaikovskii, V. I.; Stepanov, S. A. Identification of ε-Fe2O3 nano-phase in borate glasses doped with Fe and Gd. *J. Magn. Magn. Mater.* **2016**, *401*, 880−889.

https://doi.org/10.1021/acs.nanolett.1c03767
Nano Lett. 2021, 21, 9780−9788